Author's response to Review RC1 by Emmanuel Dekemper

We are very grateful for the constructive comments of Emmanuel Dekemper, which led to a very valuable extension of the manuscript. As a major point, we added the retrieval of SO2 CDs from apparent absorbances determined with the prototype instrument, which indicates the possibility of calibration free measurements.

In the following, we will answer the individual comments. For clarity we numbered them from 1) to 6) (bold font). The original reviewer comment is set in italic font, the authors' response in normal font.
We add the two sections (Sect 2.2 and Sect 4) and four Figures (1, 6, 7, 8), containing the major changes to the end of this file.

Specific comments/questions:

1)

It is true that the concept of aligning the transmission comb of the FPI with the periodic structures of the absorption cross-section of species has been described by the author in an earlier paper. However, I would have liked to see a bit more description here as well. For instance, the radiometric model of the measurements described in section 2.2 should make clearer that the measured signals I_A or I_B are made out of photons captured by each transmission peak of the FPI at the same time. Equation (5) could emphasize this by expressing I as the result of this summation process. Alternatively, one could bring equation (6) into section 2.2.

This is a good point. We extended Section 2.2 by a new Equation (Eq. 6), clarifying that I_A and I_B are spectral radiances integrated over the FPI spectral transmission interval. Furthermore, we added Fig. 1c in order to clarify the detection principle and also to visualize the optimisation of the instrument parameters for the individual trace gases (also regarding comment 2a).

2)

a) *Figures 2, 3, and 4 show a possible setting of the FPI targeting a different species respectively. One can imagine that the performance of the measurement method is strongly determined by the capability of finding the best "position" of the FPI comb in order to maximize the correlation. I found that this could have been pointed out and discussed in more details, by showing for instance how evolves this correlation as a function of a spectral displacement of the comb.*

b) *For instance, by looking at figure 4 (NO2), one observes that one of the FPI peaks of the off channel actually captures a relatively high absorption. This sounds like a suboptimal configuration whose impact could have been dealt with.*

a) This point is largely covered by our response to comment 1). The best "position" (d_A and d_B) are also indicated in Fig. 1c, representing the strongest optical density modulation.

b) Indeed the correlation of optimized FPI transmission spectrum and spectral trace gas absorption doesn't look optimal to the eye for the case of NO_2. This is because, the strong absorption band of NO_2 at around 425 to 450 nm are not equidistant. This results in a lower sensitivity, compared for example to a measurement setup where a single FPI transmission

peak is isolated and tuned to maximum and minimum absorption (e.g. at 435nm and 438nm). However, regarding the signal to noise ratio, which is also dependent on the total transmission of the instrument and cross interferences with other gases our proposed setup shows a optimal performance for our boundary conditions. There might be different optimal settings for other scenarios (e.g. a scenario with low NO_2 levels but high scattered sunlight radiances). We added the following explanation to Sect. 3.2:

'The absorption bands of NO_2 are not ideally periodic in the chosen wavelength window. Therefore at first glance they appear to be non-ideal for FPI correlation. The apparent absorbance, however, is still reasonably high with extremely low cross interferences to water vapour and O_4. This demonstrates, that periodical absorption structures are ideal but not necessary for FPI Correlation Spectroscopy. For a different measurement scenario (here we optimised for stack and ship emissions, see above) there might also be a better choice for instrument parameters. For instance for a high radiance and low NO_2 scenario one might use a single FPI transmission peak on the NO_2 absorption band at ~435 nm (as setting A) and at ~438nm (as setting B) in order to increase the sensitivity (see Fig. 4).'

3)

The determination of the CD eventually depends on the knowledge of the effective differential cross-section as shown in eq. (5). However, the way to determine this quantity is not discussed. With the actual instrument, will there be sufficient knowledge of the FPI transmission curve and of the BPF to compute it from a high resolution cross-section dataset? Or will it be necessary to measure it in the lab?

Depending on the knowledge of instrument parameters the instrument function can be modelled and used, together with a simple atmospheric radiation model, to determine CDs from apparent absorbances. We added an explanation to Sect. 2.2 and performed the CD calculation for our prototype data in Sect. 4.2. (see response to comment 4).

4)

The field experiment shows encouraging results, although it does not go up to comparing SCDs retrieved by the FPI-based instrument with the ones obtained from the classical grating-based instrument. As a reader, one immediately wonders why it is like that. Is it because there is no a priori knowledge of the effective differential cross-section (see point before), or because no clear sky measurement could be made at the time of the measurements?

This is a very good comment that led us to calculate SO_2 CDs from the apparent absorbance data, without the use of data provided by the co-aligned DOAS spectrograph. The possibility of calibration free measurements that could be shown to work pretty well for our SO_2 study constitutes another substantial advantage of our FPI-technique.
Section 4 was subdivided into 3 parts: In '4.1 Sensitivity and ozone interference' the proof of concept study is introduced and the correlation of apparent absorbance with DOAS CDs as well as the ozone interference are presented. In '4.2 Calculation of SO_2 CDs by modelling effective absorption cross sections' the model is described and the results of the retrieved FPI CDs are validated with the DOAS data. The outlook to the imaging application is given in '4.3 Imaging'.
In addition to the changes in Section 4, we added the following sentence at the end of the introduction:

'Further, we show that SO_2 CDs can be accurately retrieved from the recorded data without calibration (Sect. 4).'

And we added the explanatory text to the conclusions:

'Further, SO_2 CDs could directly be calculated from the instrument model and a very simple radiative transfer model very accurately and with a ~10% uncertainty of the sensitivity. This indicates that CDs can be retrieved directly from the FPI radiance data without calibration.'

In order to further clarify the measurement, we included the reference (zenith sky) measurement into the time series in Fig. 6. It was taken a few minutes before the plume measurement.
Finally, we removed the dashed grey line labelled with 'simulation' in Fig. 7 and added the result of the FPI CD calculations in an additional Fig. 8.

5)

In the discussion of the results of the field experiment, there is time spent on the interference by O3. However, in absence of any attempt to retrieve the SO2 CD from the FPI-based measurements, it is difficult to adhere to the conclusions of the author about a relative insensitivity to O3. On the other side, if this sensitivity is more robustly confirmed, this aspect is an important asset compared to the widespread SO2 cameras, and emphasized further.

We address this point in our response to comment 4) and by the related changes in the manuscript.

6)

In section 3, there are some inconsistencies between the text and Table 1 which it is referring to. Furthermore, the paragraph is not making it completely clear that the selected CDs are actually detection limits. In particular, for NO2, a value of 1e16 is clearly not the maximum that can be observed above a smokestack, hence it must be a detection limit... This is however better stated in the caption of Table 1.

This is true. We added 'required detection limit of' in the brackets containing the detection limits in the text in Sect. 3. We also corrected the NO_2 CD assumed for stack emission NO_2 cross sensitivities of 1e16 to 1e17 molec cm^{-2} in the text. The simulation was done for 1e17 molec^{-2} (see Tab. 1 and Fig. 2).
We additionally changed the NO_2 CD in the visualisation of the differential optical density in Fig. 4a from 1e17 to 1e16 molec cm^{-2}. That way, all the Figures (Fig. 2, 3, 4) visualise the spectral differential optical density of the target trace gas for the respective target detection limit.

Technical corrections:
• p.2,L.21: repeated "by column"   corrected as proposed
• p.2,L.22: replace "rather high" by "rather large" or "rather long" corrected as proposed
• p.2,L.27: add a comma after "imaging techniques"   corrected as proposed
• p.3,L.5: replace "Due to" by "Thanks to"   corrected as proposed
• p.3,L.11: add commas before and after "for the three gases"   corrected as proposed
• p.3,L.12: replace "by around" by "about"   corrected as proposed

• *p.4,L.1: remove "a stable"*   corrected as proposed
• *p.5,L.28: "calculated" is misspelled*   corrected as proposed
• *p.7,L.15: remove the comma after "this illustrates"*   corrected
• *p.10,L.6-7: the end of the sentence is very clear.* corrected: removed 'and' before 'trace gases'

We performed the suggested technical corrections.

Author's response to Review RC2 by Anonymous Referee #2

We kindly thank the anonymous referee for the helpful comments. In the following, we repeat the reviewer comment in italic font and answer in regular font at points we find appropriate.

This paper mostly presents a theoretical investigation of the applicability of Fabry Perot interferometers (FPIs) for the fast imaging of atmospheric trace gases, of high relevance for the visualization and quantitative assessment of localized emission sources of molecules such as SO2, BrO and NO2. The study is essentially a follow-up from study by Kuhn et al. (2014) already published in AMT and where the principle and advantages of the approach are described. Here, the authors concentrate on simulations aiming at demonstrating the selectivity of the FPI correlation spectroscopy for three potential target gases: SO2, BrO and NO2. In comparison to more traditional atmospheric trace gas imaging techniques which generally only use a set of band pass filters, the FPI correlation spectroscopy is found to be highly selective, allowing to drastically reduce cross interferences with other absorbing species while maintaining high sensitivity. In short, the method seems to be very promising. The approach used for the simulations is convincing and clearly described.

In my opinion, the manuscript is overall of excellent quality, well written and concise. However, the proof of concept presented at the end of the study is a bit disappointing. One would have expected to see first results from real images. Instead only a one-pixel prototype is shown, and only applied to SO2 retrieval (which arguably is the easiest case). It is claimed that the one-pixel prototype can "easily" be transferred in a fullframe imaging instrument, however this is not demonstrated. At minimum, the authors should explain why this transfer was not attempted in the present study and what are the possible difficulties that may need to be addressed.

We were focussing our study on the applicability of the FPI-technique to further trace gases, rather than to the implementation of an imaging prototype (although the latter goal still has high priority in our research). The proof of concept was carried out with a one pixel prototype because it can easily be coaligned with a DOAS instrument for validation and thereby allows straightforward and robust validation of the presented technique.

Despite this weakness, I think that the study remains very interesting, show a good degree of innovation (first demonstration of the potential of the technique for other species than SO2) and therefore it should be published in AMT.

In fact, my only serious reservation, concerns the estimation of the added performance of the FPI correlation spectroscopy in comparison to a traditional hyperspectral imaging system (as used for imaging DOAS). Based on existing CMOS or CCD detectors coupled to grating spectrometers (commonly used in the DOAS community), and assuming hyperpixels of 100 micron size, experience shows that typically 1.5 Me-/sec/pixel can be accumulated in the visible range under normal illumination conditions. On this basis, one can estimate that a full image of 100 x 100 spatial pixels (or even 200 x 200) could potentially be recorded in a few seconds of time (using e.g. an integration time of 50 msec/hyperspectral line) leading to a S/N ratio of approximately 250 (corresponding to a NO2 dSCD uncertainty of about 5e15 molec/cm2). This level of performance is in fact very close to the performance announced in Table 3, and therefore I believe that the factor 100 announced in the text is rather optimistic (at least for a FPI system using a telecentric optics as assumed here). Of course the real proof will have to wait

for actual measurements and I look forward to see more of such measurements being attempted and published in the near future.

We thank the reviewer for this valuable comment. The 'two orders of magnitude' are mentioned in a rough comparison of the BrO simulation results for the FPI technique and an approximate exposure time of a common MAX-DOAS setup (which is not optimised for this kind of imaging measurement). Manago et al. (2018) recently published an article introducing hyperspectral imaging measurements of NO_2. They achieve a detection limit of ~1e16molec cm^{-2} in 12s exposure with a spatial resolution of 480x640 pixels, binned 3 by 3 (i.e. effectively 160x213 pixels). This is indeed only a factor 2.2 slower than we calculated for our telecentric setup for the FPI technique. If we applied the non-telecentric setup introduced in Kuhn et al. (2014) we would increase the light throughput by a factor of 32 and therefore end up with a ~70 times faster setup.

To make this point clearer in the manuscript we made the following changes:

In the introduction, we added the reference of Manago et al. (2018) and the sentence:

'Recently, Manago et al. (2018) reported NO_2 measurements with an hyperspectral camera based on the Imaging DOAS technique with considerably higher spatial resolution (~0.08 Hz).'

We changed the last part in Sect. 3.2 to:

'When comparing to corresponding DOAS measurements the enormous increase of spatio-temporal resolution becomes evident. A state of the art DOAS measurement takes around 1s to reach a detection limit of $1x10^{14}$ molec cm^{-2} BrO for one spatial pixel. To scan the ca. 2600 pixels of the assumed BrO image would take 2600s. This is, however, a comparison with an instrument that is not optimised for this kind of imaging measurements. Manago et al. (2018) recently recorded NO_2 images with a hyperspectral camera, based on imaging DOAS. A detection limit around $1x10^{16}$ molec cm^{-2} NO_2 is reached with a spatial resolution of 480 by 640 pixels and 3 by 3 pixel binning with 12 s $frame^{-1}$. This is only a factor of 2.2 slower than our calculation for the telecentric setup. By applying the standard optics introduced in Kuhn et al. 2014, (i.e. not a telecentric optics), the light throughput is increased by another factor of 32. Therefore, theoretically, the FPI technique can be by a factor of ~70 times faster. Of course this values always depends on the size of the assumed instrument optics. Our results show that FPI Correlation Spectroscopy can be about two orders of magnitude faster than conventional DOAS measurement while maintaining a similar degree of selectivity and interference suppression.
The presented results of the exemplary calculations for SO_2, BrO and NO_2 suggest that FPI Correlation Spectroscopy can also be implemented for other trace gases with similarly strong and structured absorption, such as e.g. O_3, HCHO, IO, or OClO.'

We also mentioned the above factor of 32 in Sect 4 of our manuscript:

'Alternatively, the FPI could be placed in front of the lens using the full clear aperture and the full aperture angle of the FPI and the optics, increasing the light throughput by a factor of 32 (Kuhn et al., 2014).'

Towards imaging of atmospheric trace gases using Fabry Pérot Interferometer Correlation Spectroscopy in the UV and visible spectral range

Jonas Kuhn[1,2], Ulrich Platt[1,2], Nicole Bobrowski[1,2], and Thomas Wagner[2]

[1]Institute of Environmental Physics, University of Heidelberg, Germany
[2]Max Planck Institute for Chemistry, Mainz, Germany

Correspondence: J. Kuhn (jkuhn@iup.uni-heidelberg.de)

Abstract. Many processes in the lower atmosphere including transport, turbulent mixing and chemical conversions happen on time scales of the order of seconds (e.g. at point sources). Remote sensing of atmospheric trace gases in the UV and visible spectral range (UV/Vis) commonly uses dispersive spectroscopy (e.g. Differential Optical Absorption Spectroscopy, DOAS). The recorded spectra allow for the direct identification, separation and quantification of narrow band absorption of trace gases. However, these techniques are typically limited to a single viewing direction and limited by the light throughput of the spectrometer setup. While two dimensional imaging is possible by spatial scanning, the temporal resolution remains poor (often several minutes per image). Therefore, processes on time scales of seconds cannot be directly resolved by state of the art dispersive methods.

We investigate the application of Fabry- Pérot Interferometers (FPIs) for the optical remote sensing of atmospheric trace gases in the UV/Vis. By choosing a FPI transmission spectrum, which is optimised to correlate with narrow band (ideally periodic) absorption structures of the target trace gas, column densities of the trace gas can be determined with a sensitivity and selectivity comparable to dispersive spectroscopy, using only a small number of spectral channels (FPI tuning settings). Different from dispersive optical elements, the FPI can be implemented in full frame imaging setups (cameras), which can reach high spatio-temporal resolution. In principle, FPI Correlation Spectroscopy can be applied for any trace gas with distinct absorption structures in the UV/Vis.

We present calculations for the application of FPI Correlation Spectroscopy to SO_2, BrO and NO_2 for exemplary measurement scenarios. Besides high sensitivity and selectivity we find that the spatio temporal resolution of FPI Correlation Spectroscopy can be more than two orders of magnitude higher than state of the art DOAS measurements.

As proof of concept we built a one-pixel prototype implementing the technique for SO_2 in the UV. Good agreement with our calculations and conventional measurement techniques are demonstrated and no cross sensitivities to other trace gases are observed.

1 Introduction

Within the last decades, progress in optical remote sensing of atmospheric trace gases led to a better understanding of many important processes including air pollution, ozone and halogen chemistry, and the evolution of volcanic plumes. Narrow band structures in the trace gas molecule's absorption spectrum are used to identify and quantify the amount of a trace gas integrated along a line of sight, i.e. its column density (CD, typically in units of $\mathrm{molec\,cm^{-2}}$) and to separate its absorption signal from interfering gas absorptions and scattering processes.

Differential Optical Absorption Spectroscopy (DOAS, see Platt and Stutz, 2008, for details) has become a well established technique for atmospheric trace gas remote sensing in the UV/Vis with high sensitivity (detection limits within the ppb to ppt range for atmospheric light paths of a few kilometers). A spectrometer and a telescope with narrow field of view (FOV) are used to record spectra $I(\lambda)$ of scattered sunlight, which are compared to a reference spectrum $I_0(\lambda)$. Beer Lambert's law describes the corresponding spectral optical density $\tau(\lambda)$ with $\sigma_i(\lambda)$ and $c_i(l)$ being the absorption cross section and the concentration of trace gas species i along a line of sight L, respectively:

$$\tau(\lambda) = -\log\frac{I(\lambda)}{I_0(\lambda)} = \int\limits_0^L \sum_i \sigma_i(\lambda)c_i(l)\mathrm{d}l + \text{scattering at molecules and aerosols} \tag{1}$$

Atmospheric UV/Vis optical densities are dominated by trace gas absorption and scattering processes at air molecules or aerosols. The known absorption cross sections of the trace gases together with a polynomial, which accounts for the broad band absorption and scattering effects are fitted to the measured spectral optical density. The fit coefficients represent the CDs $S_i = \int_0^L c_i(l)\mathrm{d}l$, i.e. the integrated trace gas concentration along the light path difference of $I(\lambda)$ and the reference $I_0(\lambda)$. In principle, spatial distributions of trace gases (images or height profiles) can be recorded by scanning of viewing angles with a narrow FOV telescope (e.g. Multi-Axis DOAS, Hönninger et al., 2004). More complicated optical setups allow to record spectra of an entire image column at once by using a two dimensional detector array (e.g. Imaging DOAS, Lohberger et al., 2004). Images can then be recorded by column (push broom) scanning. The acquisition times of these techniques used to be are rather large (often several minutes per image or profile for typical trace gas CDs) limiting their application to processes that are spatially homogeneous on that time scale or processes with very high trace gas CDs. Recently, Manago et al. (2018) reported NO_2 measurements with an hyperspectral camera based on the Imaging DOAS technique with considerably higher spatial resolution ($\sim 0.08\,\mathrm{Hz}$).

Determination of two dimensional atmospheric trace gas distributions with high time resolution at time scales of the order of seconds, i.e. fast imaging of atmospheric trace gases is possible with techniques recording all spatial pixels of an image at once for a low number of spectral channels (see e.g. Platt et al., 2015). This allows studying phenomena which are not accessible to conventional scanning methods. With fast trace gas imaging techniques, sources and sinks of trace gases can be identified and quantified on much smaller spatial and temporal scales than with conventional remote sensing techniques. This allows for instance to gain insight into small scale mixing processes and to distinguish chemical conversions from transport.

Most of the presently used atmospheric trace gas imaging schemes either use a set of two band pass filters (e.g. SO_2 Camera, $\sim 1\,\mathrm{Hz}$ for volcanic emissions, see e.g. Mori and Burton, 2006; Bluth et al., 2007; Kern et al., 2010; Platt et al., 2018) or a

tuneable band pass filter as wavelength selective element (e.g. NO$_2$ Camera, $\sim 3\,\mathrm{min}$ per image for stack emissions of power plants Dekemper et al., 2016). These techniques either involve intricate optical set-ups with low light throughput or yield a rather coarse spectral resolution which might result in strong cross interferences (see e.g. Lübcke et al., 2013; Kuhn et al., 2014).

5   Here we study the application of Fabry Pérot Interferometers (FPIs) as wavelength selective elements for trace gas imaging in the UV/Vis. The periodic FPI transmission spectrum is matched to the spectral absorption structures of trace gases that often show a similar periodicity. Thanks to the high correlation of the transmission spectrum of the wavelength selective element and the trace gas absorption spectrum a high sensitivity can be reached and cross interferences with other absorbers are minimized, even if only a small number of spectral channels (FPI tuning settings) is used (see Kuhn et al., 2014, and

10   the discussion in Sect. 3.2 below). Air spaced FPI etalons are very robust devices and allow for simple optical designs that can easily be implemented in imaging sensors. We present a model study on the sensitivity and selectivity of FPI Correlation Spectroscopy applied to SO$_2$, BrO and NO$_2$ (Sect. 3). For exemplary measurement scenarios, we infer the possible spatio-temporal resolution of these measurements for a specific instrument implementation. We find that, for the three gases, imaging with spatio-temporal resolutions about two orders of magnitude higher than state of the art methods should be possible. In

15   addition, we present a proof of concept study of the technique for volcanic sulphur dioxide (SO$_2$), validating the expected high accuracy and sensitivity of the technique with a one pixel prototype instrument. ==Further, we show that SO$_2$ CDs can be accurately retrieved from the recorded data without calibration (Sect. 4).==

2   Fabry Pérot Interferometer Correlation Spectroscopy

2.1   Fabry Pérot Interferometer

20   The FPI is a fundamentally very simple optical device, known for more than a century (e.g. Perot and Fabry, 1899). In principle, it consists of two plane parallel surfaces each with reflectance R, separated by a distance d (see Fig. 1). The medium between the plates has the index of refraction n. Incident light (angle of incidence α) is split up in partial beams with different optical path lengths between the two surfaces. Due to interference of the transmitted partial beams, the spectral transmission of the FPI is characterised by periodic transmission peaks, referring to constructive interference. For high enough orders of

25   interference, the free spectral range (FSR) Δ_λ between two transmission peaks in units of wavelength λ is approximately given by:

$$\Delta_\lambda(\lambda) \approx \frac{\lambda^2}{2nd\cos\alpha} \tag{2}$$

The finesse F of a FPI represents the ratio of FSR to the full width half maximum (FWHM) δ_λ of a transmission peak:

$$F = \frac{\Delta_\lambda}{\delta_\lambda} \tag{3}$$

30   The finesse is a measure for the number of effectively interfering partial beams and therefore increasing with the surface reflectance. However, it is also depending on the alignment and quality of the surfaces.

The spectral transmission as a function of λ and the FPI's instrument parameters is given by:

$$T_{FPI}(\lambda) = \left[1 + \frac{4R}{(1-R)^2} \sin^2 \left(\frac{2\pi dn \cos \alpha}{\lambda} \right) \right]^{-1} \qquad (4)$$

Despite its simple design, the challenge in manufacturing FPI devices lies in creating set-ups keeping d stable to a fraction of a wavelength across the effective aperture.

2.2 Detection principle

The concept of using FPI correlation to detect atmospheric trace gases is described in Kuhn et al. (2014). The correlation of periodic absorption structures of atmospheric trace gases and the FPI transmission is exploited. An apparent absorbance $\tilde{\tau}_i$ of a trace gas i is calculated from the optical densities of an on-band τ_A and off-band τ_B channel:

$$\tilde{\tau}_i = \tau_A - \tau_B = \log \frac{I_{A,0}}{I_A} - \log \frac{I_{B,0}}{I_B} = (\overline{\sigma}_{A,i} - \overline{\sigma}_{B,i}) S_i = \Delta\overline{\sigma}_i S_i \qquad (5)$$

S_i denotes the CD of a trace gas i. For the on-band channel, the spectral pattern of the FPI transmittance is chosen to correlate with the absorption band structure of the target trace gas, while for the off-band channel the FPI is tuned to show minimum correlation with the target trace gas absorption (see Fig. 1). The apparent absorbance is - for low trace gas optical densities - proportional to the CD of the trace gas. The proportionality is $\Delta\overline{\sigma}$, representing the difference of the effective absorption cross section seen by channel A and channel B. The optical densities τ_k are calculated from measured radiances I_k transmitted by the FPI in a setting $k = A, B$:

$$I_k = \int_{\Delta\lambda} I(\lambda) \cdot T_{FPI,k}(\lambda) \, d\lambda \qquad (6)$$

$I_{k,0}$ denotes the reference radiance without the target trace gas in the light path. In practice, a wavelength range $\Delta\lambda$ of high correlation of spectral trace gas absorption and FPI transmission is preselected with a band pass filter (BPF). Within this spectral range the FPI physical parameters are optimised. Figure 1c shows the optical density of BrO seen through an FPI with varying surface displacement d. The maximum difference between maximum and minimum optical density determine the FPI settings A and B. In addition, the Finesse is chosen to maximise the signal to noise ratio.

Here we apply FPI Correlation Spectroscopy for passive imaging of a trace gas in the atmosphere. This means that the light source is scattered sky radiation that is measured within an imaging FOV (e.g. 20° aperture angle). We assume in the following that a reference I_0 (i.e. a part without trace gas) is always present within the image, so that S denotes the differential trace gas CD compared to that reference.

The proportionality $\Delta\overline{\sigma}$ of apparent absorbance $\tilde{\tau}$ and trace gas CD S (see Eq. 5) can be calculated from literature absorption cross sections of the target trace gas, a background spectrum $I_0(\lambda)$ and a modeled instrument transfer function (see Sect. 3.1 and 4.2). Alternatively, $\Delta\overline{\sigma}$ can be determined through calibration (see e.g. Lübcke et al., 2013; Sihler et al., 2017).

4

3 Model study for SO_2, NO_2 and BrO

FPI Correlation Spectroscopy can be applied to every trace gas species that yields sufficiently strong spectral absorption struc-
tures in the regarded wavelength range. In this section we present exemplary model studies for imaging of SO_2, NO_2 and BrO.
For each target trace gas we regard a typical exemplary measurement scenario (Tab. 1). For the target species BrO and SO_2 we
use typical measurement scenarios of volcanic emissions in the UV spectral range. For SO_2 we assume CDs that are typically
measured in volcanic plumes of a comparably weak volcanic emitter or an already highly diluted plume (required detection
limit of 1e17 $\mathrm{molec\,cm^{-2}}$, see Tab. 1). We additionally chose a high and probably disturbing NO_2 CD (1e17 $\mathrm{molec\,cm^{-2}}$) in
oder to make the scenario also applicable to SO_2 measurements at e.g. ship or industrial stack emissions. Existing filter based
SO_2 cameras are subject to strong cross interferences in this CD range (see e.g. Lübcke et al., 2013; Kuhn et al., 2014). In the
scenario for BrO we assume a relatively strong but not uncommon volcanic emitter, with BrO mixing ratios of tens to hundreds
ppt within the plume (required detection limit of 1e14 $\mathrm{molec\,cm^{-2}}$, see Tab. 1) and high SO_2 CDs (3e18 $\mathrm{molec\,cm^{-2}}$). Gra-
dients in the BrO distributions can give insight into in-plume halogen chemistry (see e.g. Bobrowski et al., 2007; von Glasow,
2010; Roberts et al., 2014). The NO_2 scenario (blue spectral range) is applicable to measurements of stack emissions at e.g. a
coal power plant (see e.g. Dekemper et al., 2016) but also to local gradients induced by traffic (required detection limit of 1e16
$\mathrm{molec\,cm^{-2}}$, see Tab. 1).

We calculate the sensitivities and study the cross interference of the apparent absorbance with other atmospheric absorbers
for typical differential CDs for the respective measurement scenario. Table 1 lists the assumed differential CDs of the trace
gases absorbing in the same spectral range as the trace gases under investigation. For these potentially interfering trace gases
we chose relatively high values, so that the indicated cross interferences correspond to upper limits. The listed CDs represent
differential CDs across a typical image FOV ($\sim 20°$), assuming that within the image always a reference region I_0 without the
target trace gas is present.

In a second step, we calculate the corresponding photon budgets in order to infer the approximate achievable spatial and tem-
poral resolution of the respective imaging measurement.

3.1 Description of the Model

The apparent absorbance is calculated from radiances I_k (in $[\mathrm{photons\,s^{-1}\,mm^{-2}\,sr^{-1}}]$) of scattered solar radiation transmitted
by the respective spectral channel $k = A, B$ (on-band and off-band FPI setting) :

$$I_k = \int d\lambda\, I_0(\lambda) e^{-\sum_i \sigma_i(\lambda) S_i} T_{FPI,k}(\lambda) T_{BPF}(\lambda) \tag{7}$$

A spectrum recorded at a clear day in Heidelberg with a solar zenith angle of 73° (160° relative solar azimuth, 89° viewing
zenith angle) was used to approximate the spectral radiance $I_0(\lambda)$. $I_0(\lambda)$ was scaled with scattered sky radiance measurements
from (Blumthaler et al., 1996). The radiance measurements were performed in Innsbruck in February, 1995 with a solar zenith
angle of 68°. For our calculations we used the values for 180° relative solar azimuth and 70° viewing zenith angle. S_i is the

CD of an absorbing gas species i with spectral absorption cross section $\sigma_i(\lambda)$. $T_{FPI,k}$ is the FPI transmittance in configuration k (see Eq. (4)) and T_{BPF} the transmittance of the BPF isolating the measurement wavelength range for the respective target trace gas. T_{BPF} was modeled with a higher order Gaussian function:

$$T_{BPF}(\lambda) = P e^{-\left(\frac{(\lambda_{BPF}-\lambda)^2}{2c^2}\right)^p} \tag{8}$$

with a FWHM of

$$\delta_{\lambda,BPF} = 2c\sqrt{2(\log 2)^{\frac{1}{p}}} \tag{9}$$

P describes the peak transmission at a central wavelength λ_{BPF}. An order $p = 6$ was used to approximate interference filter transmission profiles.

With Eq. (5) and the intensities I_k from Eq. (7), the apparent absorbance $\tilde{\tau}_i$ can be calculated, allowing to study the sensitivity and selectivity of the detection of a trace gas i for given FPI instrument settings.

In addition, we approximate the respective detection limits based on photon shot noise. In order to calculate the number of photons that reach the detector of the imaging device, we need to know the etendue (product of entrance area A and aperture solid angle Ω) of the employed optics. Kuhn et al. (2014) suggest several optical setups for FPI Correlation Spectroscopy imaging implementations. Here, we chose the setup in which, with help of an image space telecentric optics (see Fig. 5), the incident radiation from the imaging FOV is parallelised before traversing the FPI and BPF. In order to avoid strong blurring of the FPI transmission spectrum due to different incidence angles, the divergence Θ of the light beams traversing the FPI should not be much larger than $\Theta = 1°$. With a lens of focal length f this condition limits the maximum aperture radius a to:

$$a = f \tan\frac{\Theta}{2} \tag{10}$$

The FPI clear aperture radius a_{FPI} determines the imaging FOV aperture angle

$$\gamma_{FOV} = 2\arctan\frac{a_{FPI}}{f} \tag{11}$$

The etendue per pixel E_{pix} is determined by the spatial resolution of the recorded image, which can be varied by binning individual pixels. For n_{pix} being the number of pixels along a column of a square detector array, the approximate etendue per pixel of the instrument is:

$$E_{pix} = A_{pix}\Omega_{pix} \approx a^2 \sin^2(\frac{\gamma_{FOV}}{2n_{pix}})\pi^2 \tag{12}$$

The detectors quantum efficiency and losses within the optics are considered to be not wavelength dependent in the regarded spectral ranges and combined in a loss factor η. We chose a somewhat lower loss factor for the UV (0.25 for SO_2 and BrO) compared to the Vis (0.5 for NO_2) due to the higher quantum efficiency of commonly used detectors. Each FPI channel (on-band and off-band setting) requires one image acquisition. We assume a photon electron shot noise limited measurement, where for an exposure time Δt the number of counted photo electrons per pixel and image is

$$N_{phe,pix} = I E_{pix}\eta\Delta t \tag{13}$$

with an uncertainty of $\Delta N_{phe,pix} = \sqrt{N_{phe,pix}}$. The uncertainty in the apparent absorbance $\tilde{\tau}$ is then

$$\Delta\tilde{\tau} \approx \sqrt{\frac{2}{N_{phe,pix}}} \tag{14}$$

assuming the intensities I_k for the two FPI settings $k = A, B$ are similar and that the reference intensities $I_{0,k}$ have to be recorded only once.

5   Note, that the used sky radiances, loss factors and dimensions of the optics (see Tab. 2) represent conservative assumptions. For instance the light throughput could be enhanced by more than an order of magnitude by choosing a different optical setup (see Kuhn et al., 2014). There, the FPI is placed in front of the lens using the full clear aperture and the full aperture angle of the FPI and the optics. Each viewing direction of the FOV, however, will have a different incidence angle onto the FPI and therefore a different FPI transmission spectrum, which has to be accounted for in the data analysis. Alternatively, simply a larger FPI

10   could be used. The results of the following calculations for the image space telecentric optics, therefore, represent lower limits of the performance.

3.2   Results of the simulations

The FPI Correlation Spectroscopy technique allows for numerous different realisations regarding the used spectral window and FPI instrument parameters that can be chosen according to e.g. measurement conditions or availability of optical components

15   (FPI, BPF). Here, we identified spectral windows in which the target trace gas absorption cross sections exhibit approximately periodic structures and appropriate FPI parameters were determined in order to maximise the correlation of FPI transmission and trace gas absorption according to the procedures described in Kuhn et al. (2014). Table 2 lists the parameters for the exemplary setups we use in this work.

The results for SO_2, BrO and NO_2 are summarized in Fig. 2, 3 and 4, which show the differential optical densities of the

20   target trace gas and the potentially interfering trace gases for the respective measurement wavelength ranges (panels a). In the lower panels, the transmitted spectral radiances of the respective FPI spectral channels (on-band, off-band) are plotted. The SO_2 and NO_2 trace gas optical density clearly dominate the total differential optical density for the targeted detection limits. For BrO the other trace gases exhibit differential optical depths on the same order of magnitude as BrO. In the b) panels of the same figures, the respective simulated calibration curves are plotted, where the dashed lines indicate the impact of the

25   individual interferring gases for the assumed amounts. For all three gases these impacts are well below the targeted detection limit. Especially for the case of BrO this illustrates how FPI Correlation Spectroscopy can effectively separate the absorption structure of a single trace gas from a multitude of trace gas optical densities of the same order of magnitude. By using more than two FPI settings, the selectivity can be enhanced even further.

The absorption bands of NO_2 are not ideally periodic in the chosen wavelength window. Therefore, at first glance they appear

30   to be non-ideal for FPI correlation. The apparent absorbance, however, is still reasonably high with extremely low cross interferences to water vapour and O_4. This demonstrates, that periodical absorption structures are ideal but not necessary for FPI Correlation Spectroscopy. For a different measurement scenario (here we optimised for stack and ship emissons, see above) there might also be a better choice for instrument parameters. For instance for a high radiance and low NO_2 scenario one might

use a single FPI transmission peak on the NO_2 absorption band at $\sim 435\,\text{nm}$ (as setting A) and at $\sim 438\,\text{nm}$ (as setting B) in order to increase the sensitivity (see Fig. 4).

Table 3 summarises the results of the photon budget calculations. We calculated the maximum possible spatial resolution of the imaging measurement for a $10\,\text{s}$ exposure time and the instrument parameters listed in Tab. 2. For this, spatial pixels are co-added until the targeted detection limit was reached. We find that for the targeted detection limits the spatial resolutions of the imaging measurements for the chosen parameters are 226 by 226 pixels for SO_2, 51 by 51 pixels for BrO and 252 by 252 pixels for NO_2 for a temporal resolution of $10\,\text{s}$. The temporal resolution could be enhanced at the expense of the spatial resolution or vice versa. For instance, cutting the linear spatial resolution in half (e.g. from 226 by 226 to 113 by 113 pixels for SO_2), would reduce the temporal resolution to 5s for the same detection limit.

When comparing to corresponding DOAS measurements the increase of spatio-temporal resolution becomes evident. A state of the art DOAS measurement takes around $1\,\text{s}$ to reach a detection limit of $1 \cdot 10^{14}\,\text{molec}\,\text{cm}^{-2}$ BrO for one spatial pixel. To scan the ca. 2600 pixels of the assumed BrO image would take 2600s. This is, however, a comparison with an instrument that is not optimised for this kind of imaging measurements. Manago et al. (2018) recently recorded NO_2 images with a hyperspectral camera, based on imaging DOAS. A detection limit around $1 \cdot 10^{16}\,\text{molec}\,\text{cm}^{-2}$ NO_2 is reached with a spatial resolution of 480 by 640 pixels and 3 by 3 pixel binning with $12\,\text{s}\,\text{frame}^{-1}$. This is only a factor of 2.2 slower than our calculation for the telecentric setup. By applying the standard optics introduced in Kuhn et al. (2014), the light throughput is increased by another factor of 32. Therefore, theoretically, the FPI technique can be by a factor of ~ 70 times faster. Of course these values always depend on the size of the assumed instrument optics. Our results show that FPI Correlation Spectroscopy can be about two orders of magnitude faster than conventional DOAS measurements while maintaining a similar degree of selectivity and interference suppression.

The presented results of the exemplary calculations for SO_2, BrO and NO_2 suggest that FPI Correlation Spectroscopy can also be implemented for other trace gases with similarly strong and structured absorption, such as e.g. O_3, HCHO, IO, or OClO.

4 Proof of concept: Field measurements of volcanic SO_2

4.1 Sensitivity and ozone interference

The above model study on trace gas detection with FPI Correlation Spectroscopy was validated in a proof of concept field study for volcanic SO_2. In a one-pixel prototype a single photodiode was used as detector. A BPF ($\lambda_{BPF} \approx 310\,\text{nm}, \delta_{\lambda,BPF} \approx 10\,\text{nm}$) was used for the preselection of a wavelength range, where the SO_2 differential absorption is strong and approximately periodic (see Fig. 2). A FPI (air-spaced etalon from *SLS Optics Ltd.*) with a FSR of $2.1\,\text{nm}$ and a Finesse of 7 across a clear aperture of $20\,\text{mm}$ was tilted by a servo motor in order to tune it to the on-band and off-band transmission settings. The individual plates of the FPI have a finite thickness and two surfaces, the outer surfaces have an anti-reflective coating and are slightly wedged from the inner surfaces of the plates, so their influence can be neglected here. The optical setup behind FPI and BPF consists of a fused silica lens ($f \approx 50\,\text{mm}$), which projects light from a narrow FOV ($\sim 0.8°$ aperture angle) onto the photodiode.

Radiances for the on-band and off-band channel were recorded, delivering an apparent absorbance measurement with 0.42 Hz. A telescope ($\sim 0.5°$ aperture angle) was co-aligned with the one pixel FPI setup and connected to a temperature stabilized spectrometer (spectral resolution $\sim 0.8\,\mathrm{nm}$). The recorded spectra ($\sim 0.13\,\mathrm{Hz}$) were evaluated with the DOAS algorithm.

The measurement was performed at the *Osservatorio Vulcanologico Pizzi Deneri* (37.766° N, 15.017° E, 2800 m a.s.l.) at Mt. Etna on Sicily on 30 July 2017. The device was pointed towards the volcanic plume of Mt. Etna with constant viewing angle (8° viewing elevation, azimuth 280° N). A plume free part of the sky (zenith viewing direction) was used for reference measurements and recorded prior to the plume measurement. Fig. 6 shows the time series of the apparent absorbance of the FPI Correlation Spectroscopy prototype together with the SO_2 CD retrieved from the co-recorded spectra. The apparent absorbance shows high correlation with the retrieved SO_2 CD. In Fig. 7 the correlation plot is shown. For high SO_2 CDs the sensitivity of $\tilde{\tau}_{SO_2}$ decreases slightly due to saturation effects. The scatter of the values mainly originates from slight misalignment and the difference of the two narrow FOVs.

The recorded UV spectra also allow for evaluating the O_3 absorption. The lower panel of Fig. 6 shows the change of the differential O_3 CD during the measurement with respect to the reference. The observed increase of the O_3 CD by more than $4 \cdot 10^{18}\,\mathrm{molec\,cm^{-2}}$ during the plume measurement is due to the increasing stratospheric light path with increasing solar zenith angle (63.58° to 79.31° during the measurement sequence). Within an imaging FOV (of e.g. 17°) much lower differential O_3 CDs are expected (see Tab. 2), since all pixels are similarly affected by the change in O_3 background. Even with this extreme change in O_3 CD no impact on the recorded SO_2 apparent absorbances is observed.

The presented data also indicates the potential of using an additional DOAS measurement for the calibration of the apparent absorbance of an FPI imaging device. The position of the narrow FOV of a DOAS telescope pointing into the wide imaging FOV can be retrieved from time series and used for an in-operation calibration (see e.g. Lübcke et al., 2013; Sihler et al., 2017).

4.2 Calculation of SO_2 CDs by modeling effective absorption cross sections

As stated in Sect 2.2 we can also directly calculate the SO_2 CDs from the apparent absorbance $\tilde{\tau}$ by modeling the effective absorption cross sections and thereby $\Delta\overline{\sigma}_{SO_2}$. This requires knowledge about the instrument spectral transmission, the background scattered light spectrum and the SO_2 absorption cross section.

We modeled the instrument transfer function with the transmission spectrum of the used band pass filter, the calculated FPI transmission spectrum (see Sect. 3.1) and the quantum efficiency of the photodiode. The background scattered sunlight spectrum was modeled using a high resolution solar atlas spectrum according to Chance and Kurucz (2010), scaled by the wavelength to the fourth power (assuming Rayleigh scattering) and multiplied with the transmission of the total slant atmospheric ozone column. The ozone column was estimated to $2.5 \cdot 10^{19}\,\mathrm{molec\,cm^{-2}}$ using the vertical ozone column (for the measurement day according to satellite measurements, TEMIS database, Veefkind et al., 2006) multiplied with a geometric air mass factor for the average solar zenith angle during the measurement. The SO_2 absorption cross section of Vandaele et al. (2009) was used.

The largest uncertainties are the finesse of the FPI and the modeled background spectrum, where Rayleigh scattering approximation and the assumed ozone column introduce uncertainties. A finesse of about 7 is reported by the manufacturer for

perpendicularly incident radiation. For the instrument model we have to calculate the effective finesse for a divergent light ray ($\sim 0.8°$ aperture angle) for the two FPI tilt positions (around $0°$ for setting B and $5°$ for setting A, corresponding to a finesse of around 7 and 5, respectively). Since the divergent light ray reaching the detector is dependent on focal length, detector area, the alignment of the optical components and due to the uncertainty in the reflectance of the FPI we can determine the finesse

5 only with an uncertainty of $\pm 3\%$. Further we estimate an uncertainty in the background spectrum by $\pm 10\%$ in our calculation, accounting for uncertainties in atmospheric radiative transfer and ozone column.

Figure 8 shows the SO_2 CDs calculated with the described FPI model as a function of the SO_2 CDs retrieved from the DOAS spectra. We observe an excellent agreement with a slope of 0.99, an intercept of $7.5 \cdot 10^{15}\,\mathrm{molec\,cm^{-2}}$ and $R^2 = 0.96$. The uncertainties in background spectral radiance and finesse result in a uncertainty in the SO_2 sensitivity $\Delta\overline{\sigma}_{SO_2}$ of around $\pm 10\%$

10 and therefore a relative uncertainty of $\pm 10\%$ in the retrieved SO_2 CD. Here, it is important to highlight the difference between ozone interference with the apparent absorbance and the influence of an uncertainty in the total ozone column assumed in the model. The former seems to be negligible as shown by the measurements (Fig. 6) and in the model study (Sect. 3.2). The latter influences the modeled sensitivity of the measurement. This means, it introduces a small relative uncertainty to the retrieved CDs, which has almost no influence on the detection limit. The saturation effects observed for high CDs in the apparent ab-

15 sorbances (see Fig. 7), meaning the CD dependency of $\Delta\overline{\sigma}_{SO_2}$, are accounted for by the model as well. This is a very promising result, pointing towards the possibility of calibration free measurements, which would be another major advantage of the FPI Correlation Spectroscopy compared to e.g. filter based SO_2 cameras.

4.3 Imaging

20 The one pixel FPI Correlation Spectroscopy prototype, introduced in this study, can be implemented in a full frame imaging instrument. This is the major advantage of the technique compared with the DOAS technique. The imaging implementation can be achieved with e.g. the image space telecentric optical setup, used for the above calculations and shown in Fig. 5. In principle, the single pixel detector (photodiode) is replaced by a two dimensional detector array (UV sensitive for SO_2 and BrO) and an aperture stop is added in the focal plane in front of the lens. This would, however, reduce the light throughput

25 per pixel of the imaging setup compared to the one pixel prototype. Alternatively, the FPI could be placed in front of the lens using the full clear aperture and the full aperture angle of the FPI and the optics, increasing the light throughput by a factor of 32 (see Kuhn et al., 2014). This leads to a much higher light throughput, however, the incidence angle of the incident light onto the FPI and thereby the FPI transmission spectrum becomes dependent on the pixel (i.e. the viewing direction within the imaging FOV) and has to be accounted for in the data evaluation.

30

5   Conclusions

Many locally variable atmospheric processes are difficult to quantify with state of the art UV/Vis remote sensing methods (e.g. DOAS) due to the limited spatio-temporal resolution. This makes it difficult to e.g. study the emission of point sources or to separate the effects of transport and chemical conversion on local scales. Kuhn et al. (2014) proposed the FPI Correlation Spectroscopy for SO_2 in the UV wavelength range after similar approaches have been studied in infrared wavelength ranges (e.g. Wilson et al., 2007; Vargas-Rodríguez and Rutt, 2009). The major motivation is to reduce the number of spectral channels used for the trace gas detection in order to increase the spatio-temporal resolution of the measurement while maintaining its selectivity.

In a model study we investigated the sensitivity and determined the photon budget of FPI Correlation Spectroscopy for three measurement scenarios for SO_2, BrO and NO_2. For SO_2 we assumed a scenario with rather low volcanic emissions, which is also representative for industrial stack or ship emissions. For BrO a scenario with stronger volcanic emissions was assumed, with BrO mixing ratios of 10 to 100 ppt within the volcanic plume and high SO_2 CDs. The NO_2 measurement scenario represents typical stack emissions of power plants and gradients of local air pollution induced by e.g. traffic.

For all three investigated gases, cross interferences with other trace gases absorbing in the preselected spectral ranges were found to be very low, meaning that the selectivity of FPI Correlation Spectroscopy can be similar to the selectivity of conventional techniques (e.g. DOAS). In this study, we only used two FPI settings. A larger number of FPI settings could be used to further reduce possible cross interferences.

Using rather conservative assumptions regarding the intensity of the incoming radiation and the size of the instrument optics, we calculated the highest possible spatio-temporal resolution of the FPI Correlation Spectroscopy measurements for the different scenarios and found that they can be more than two orders of magnitude higher compared to state of the art DOAS measurements for the same trace gas CD. This means that in the same time period a conventional dispersive technique records a single viewing direction (i.e. a single spatial pixel), almost an entire image can be recorded with the FPI Correlation Spectroscopy. This strongly indicates that future instruments based on FPI Correlation Spectroscopy can provide unprecedented insight into short time or small scale processes in the atmosphere.

In the second part, we presented a proof of concept field study for FPI Correlation Spectroscopy applied to volcanic SO_2, which confirms the model simulations by comparing the measured apparent absorbance to SO_2 CDs retrieved by a co-aligned DOAS measurement. One particularly important finding is that, as expected from the model study, no O_3 cross interference can be observed over a large O_3 CD range. Further, SO_2 CDs could directly be calculated from the instrument model and a very simple radiative transfer model very accurately and with a $\sim 10\%$ uncertainty of the sensitivity. This indicates that CDs can be retrieved directly from the FPI radiance data without calibration.

The extension of the one pixel prototype to a camera can be accomplished comparably easily by minor modifications of the optics and by using a UV sensitive detector array and should be the aim of future studies. By replacing the FPI and the BPF, the instrument is adjusted to measure different trace gases, e.g. BrO and NO_2 according to the model calculations performed in Sect. 3.

The applications of UV/Vis FPI Correlation Spectroscopy mentioned in this work represent only some examples for trace gases and phenomena that could be studied. Beyond the volcanological application, FPI imaging can for instance be used to study SO_2 in air pollution or BrO in salt pans (see e.g. Holla et al., 2015). The technique can also be applied to other trace gases with similarly strong and structured absorption, such as e.g. O_3, HCHO, IO, or OClO.

References

Blumthaler, M., Gröbner, J., Huber, M., and Ambach, W.: Measuring spectral and spatial variations of UVA and UVB sky radiance, Geophys. Res. Lett., 23, 547–550, https://doi.org/10.1029/96gl00248, 1996.

Bluth, G., Shannon, J., Watson, I., Prata, A., and Realmuto, V.: Development of an ultra-violet digital camera for volcanic SO2 imaging, J. Volcanol. Geotherm. Res., 161, 47–56, https://doi.org/https://doi.org/10.1016/j.jvolgeores.2006.11.004, 2007.

Bobrowski, N. and Giuffrida, G.: Bromine monoxide/sulphur dioxide ratios in relation to volcanological observations at Mt. Etna 2006-2009, Solid Earth, 3, 433, 2012.

Bobrowski, N., von Glasow, R., Aiuppa, A., Inguaggiato, S., Louban, I., Ibrahim, O. W., and Platt, U.: Reactive halogen chemistry in volcanic plumes, J. Geophys. Res., 112, D06 311, https://doi.org/10.1029/2006JD007206, 2007.

Bogumil, K., Orphal, J., Homann, T., Voigt, S., Spietz, P., Fleischmann, O., Vogel, A., Hartmann, M., Kromminga, H., Bovensmann, H., Frerick, J., and Burrows, J.: Measurements of molecular absorption spectra with the {SCIAMACHY} pre-flight model: instrument characterization and reference data for atmospheric remote-sensing in the 230-2380 nm region, J. Photoch. Photobio. A, 157, 167 – 184, https://doi.org/http://dx.doi.org/10.1016/S1010-6030(03)00062-5, 2003.

Chance, K. and Kurucz, R.: An improved high-resolution solar reference spectrum for earth's atmosphere measurements in the ultraviolet, visible, and near infrared, J. Quant. Spec. Rad. Trans., 111, 1289–1295, https://doi.org/10.1016/j.jqsrt.2010.01.036, 2010.

Chance, K. and Orphal, J.: Revised ultraviolet absorption cross sections of H2CO for the HITRAN database, J. Quant. Spec. Rad. Trans., 112, 1509–1510, https://doi.org/10.1016/j.jqsrt.2011.02.002, 2011.

Dekemper, E., Vanhamel, J., Van Opstal, B., and Fussen, D.: The AOTF-based NO 2 camera, Atmos. Meas. Tech., 9, 6025, https://doi.org/https://doi.org/10.5194/amt-9-6025-2016, 2016.

Fleischmann, O. C., Hartmann, M., Burrows, J. P., and Orphal, J.: New ultraviolet absorption cross-sections of BrO at atmospheric temperatures measured by time-windowing Fourier transform spectroscopy, J. Photoch. Photobio. A, 168, 117 – 132, https://doi.org/http://dx.doi.org/10.1016/j.jphotochem.2004.03.026, 2004.

Gliß, J., Bobrowski, N., Vogel, L., Pöhler, D., and Platt, U.: OClO and BrO observations in the volcanic plume of Mt. Etna and implications on the chemistry of chlorine and bromine species in volcanic plumes, Atmos. Chem.Phys., 15, 5659–5681, https://doi.org/10.5194/acp-15-5659-2015, 2015.

Holla, R., Schmitt, S., Frieß, U., Pöhler, D., Zingler, J., Corsmeier, U., and Platt, U.: Vertical distribution of BrO in the boundary layer at the Dead Sea, Environ. Chem., 12, 438–460, https://doi.org/10.1071/EN14224, 2015.

Hönninger, G., von Friedeburg, C., and Platt, U.: Multi axis differential optical absorption spectroscopy (MAX-DOAS), Atmos. Chem. Phys., 4, 231–254, https://doi.org/10.5194/acp-4-231-2004, 2004.

Kern, C., Kick, F., Lübcke, P., Vogel, L., Wöhrbach, M., and Platt, U.: Theoretical description of functionality, applications, and limitations of SO_2 cameras for the remote sensing of volcanic plumes, Atmos. Meas. Tech., 3, 733–749, https://doi.org/10.5194/amt-3-733-2010, 2010.

Kromminga, H., Orphal, J., Spietz, P., Voigt, S., and Burrows, J. P.: New measurements of OClO absorption cross-sections in the 325-435 nm region and their temperature dependence between 213 and 293 K, J. Photoch. Photobio. A, 157, 149–160, https://doi.org/10.1016/S1010-6030(03)00071-6, 2003.

Kuhn, J., Bobrowski, N., Lübcke, P., Vogel, L., and Platt, U.: A Fabry Pérot interferometer-based camera for two-dimensional mapping of SO_2 distributions, Atmos. Meas. Tech., 7, 3705–3715, https://doi.org/10.5194/amt-7-3705-2014, 2014.

Lohberger, F., Hönninger, G., and Platt, U.: Ground-Based Imaging Differential Optical Absorption Spectroscopy of Atmospheric Gases, Appl. Opt., 43, 4711–4717, https://doi.org/10.1364/AO.43.004711, 2004.

Lübcke, P., Bobrowski, N., Illing, S., Kern, C., Nieves, J. M. A., Vogel, L., Zielcke, J., Granados, H. D., and Platt, U.: On the absolute calibration of SO2 cameras, Atmos. Meas. Tech., 6, 677–696, https://doi.org/10.5194/amt-6-677-2013, 2013.

5 Manago, N., Takara, Y., Ando, F., Noro, N., Suzuki, M., Irie, H., and Kuze, H.: Visualizing spatial distribution of atmospheric nitrogen dioxide by means of hyperspectral imaging, Appl. Opt., 57, 5970, https://doi.org/10.1364/ao.57.005970, 2018.

Mori, T. and Burton, M.: The SO2 camera: A simple, fast and cheap method for ground-based imaging of SO2 in volcanic plumes, Geophys. Res. Lett., 33, https://doi.org/https://doi.org/10.1029/2006GL027916, 2006.

Perot, A. and Fabry, C.: On the Application of Interference Phenomena to the Solution of Various Problems of Spectroscopy and Metrology, Astrophys. J., 9, 87, https://doi.org/10.1086/140557, 1899.

Platt, U. and Stutz, J.: Differential optical absorption spectroscopy, Springer, Berlin, Heidelberg, Germany, 2008.

Platt, U., Lübcke, P., Kuhn, J., Bobrowski, N., Prata, F., Burton, M., and Kern, C.: Quantitative imaging of volcanic plumes - Results, needs, and future trends, J. Volcanol. Geotherm. Res., 300, 7–21, 2015.

Platt, U., Bobrowski, N., and Butz, A.: Ground-Based Remote Sensing and Imaging of Volcanic Gases and Quantitative Determination of
15 Multi-Species Emission Fluxes, Geosciences, 8, 44, https://doi.org/10.3390/geosciences8020044, 2018.

Roberts, T., Martin, R., and Jourdain, L.: Reactive bromine chemistry in Mount Etna's volcanic plume: the influence of total Br, high-temperature processing, aerosol loading and plume–air mixing, Atmos. Chem. Phys., 14, 11 201–11 219, 2014.

Roscoe, H. K., Van Roozendael, M., Fayt, C., du Piesanie, A., Abuhassan, N., Adams, C., Akrami, M., Cede, A., Chong, J., Clémer, K.,
Friess, U., Gil Ojeda, M., Goutail, F., Graves, R., Griesfeller, A., Grossmann, K., Hemerijckx, G., Hendrick, F., Herman, J., Hermans,
20 C., Irie, H., Johnston, P. V., Kanaya, Y., Kreher, K., Leigh, R., Merlaud, A., Mount, G. H., Navarro, M., Oetjen, H., Pazmino, A., Perez-Camacho, M., Peters, E., Pinardi, G., Puentedura, O., Richter, A., Schönhardt, A., Shaiganfar, R., Spinei, E., Strong, K., Takashima, H., Vlemmix, T., Vrekoussis, M., Wagner, T., Wittrock, F., Yela, M., Yilmaz, S., Boersma, F., Hains, J., Kroon, M., Piters, A., and Kim, Y. J.: Intercomparison of slant column measurements of NO$_2$ and O$_4$ by MAX-DOAS and zenith-sky UV and visible spectrometers, Atmos. Meas. Tech., 3, 1629–1646, https://doi.org/10.5194/amt-3-1629-2010, 2010.

25 Rothman, L., Gordon, I., Babikov, Y., Barbe, A., Benner, D. C., Bernath, P., Birk, M., Bizzocchi, L., Boudon, V., Brown, L., Campargue, A., Chance, K., Cohen, E., Coudert, L., Devi, V., Drouin, B., Fayt, A., Flaud, J.-M., Gamache, R., Harrison, J., Hartmann, J.-M., Hill, C., Hodges, J., Jacquemart, D., Jolly, A., Lamouroux, J., Roy, R. L., Li, G., Long, D., Lyulin, O., Mackie, C., Massie, S., Mikhailenko, S., Müller, H., Naumenko, O., Nikitin, A., Orphal, J., Perevalov, V., Perrin, A., Polovtseva, E., Richard, C., Smith, M., Starikova, E., Sung, K., Tashkun, S., Tennyson, J., Toon, G., Tyuterev, V., and Wagner, G.: The {HITRAN2012} molecular spectroscopic database, J. Quant.
30 Spec. Rad. Trans., 130, 4 – 50, https://doi.org/http://dx.doi.org/10.1016/j.jqsrt.2013.07.002, 2013.

Serdyuchenko, A., Gorshelev, V., Weber, M., Chehade, W., and Burrows, J. P.: High spectral resolution ozone absorption cross-sections - Part 2: Temperature dependence, Atmos. Meas. Tech., 7, 625–636, https://doi.org/10.5194/amt-7-625-2014, 2014.

Sihler, H., Lübcke, P., Lang, R., Beirle, S., de Graaf, M., Hörmann, C., Lampel, J., de Vries, M. P., Remmers, J., Trollope, E., Wang, Y., and Wagner, T.: In-operation field-of-view retrieval (IFR) for satellite and ground-based DOAS-type instruments applying coincident
35 high-resolution imager data, Atmos. Meas. Tech., 10, 881–903, https://doi.org/10.5194/amt-10-881-2017, 2017.

Thalman, R. and Volkamer, R.: Temperature dependent absorption cross-sections of O$_2$-O$_2$ collision pairs between 340 and 630 nm and at atmospherically relevant pressure, Phys. Chem. Chem. Phys., 15, 15 371–15 381, https://doi.org/10.1039/C3CP50968K, 2013.

Vandaele, A. C., Hermans, C., and Fally, S.: Fourier transform measurements of SO 2 absorption cross sections: II.: Temperature dependence in the 29000–44000cm- 1 (227–345nm) region, J. Quant. Spec. Rad. Trans., 110, 2115–2126, 2009.

Vargas-Rodríguez, E. and Rutt, H.: Design of CO, CO2 and CH4 gas sensors based on correlation spectroscopy using a Fabry–Perot interferometer, Sensor. Actuat. B Chem., 137, 410–419, https://doi.org/10.1016/j.snb.2009.01.013, 2009.

5 Veefkind, J., de Haan, J., Brinksma, E., Kroon, M., and Levelt, P.: Total ozone from the ozone monitoring instrument (OMI) using the DOAS technique, IEEE T. Geosci. Remote., 44, 1239–1244, https://doi.org/10.1109/tgrs.2006.871204, 2006.

von Glasow, R.: Atmospheric chemistry in volcanic plumes, Proc. Natl. Acad. Sci., 107, 6594–6599, 2010.

Wilson, E. L., Georgieva, E. M., and Heaps, W. S.: Development of a Fabry–Perot interferometer for ultra-precise measurements of column CO2, Meas. Sci. Technol., 18, 1495–1502, https://doi.org/10.1088/0957-0233/18/5/040, 2007.
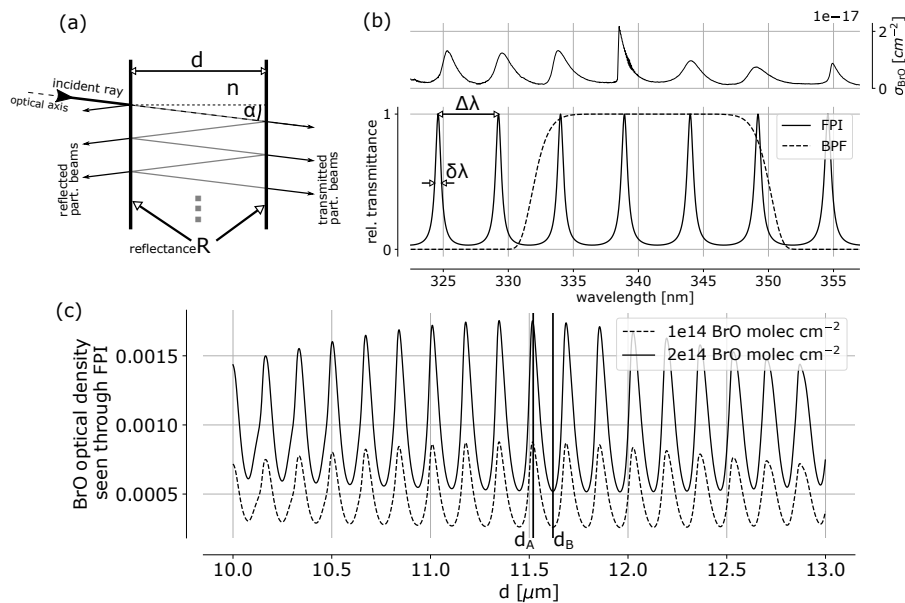
Figure 1. (a) FPI schematics indicating the splitting of incident radiation into partial beams that interfere to cause the FPI transmittance spectrum (b), which is characterised by periodic transmission maxima with a FWHM of δ_λ and a FSR of Δ_λ. The BrO absorption cross section (upper panel) shows approximately periodic structures allowing for a high correlation with spectral FPI transmittance. This leads to a modulation of the BrO optical density as seen through the FPI with changing surface displacement d (c). The apparent absorbance is the difference of the optical densities of FPI settings A and B, representing maximum and minimum correlation of FPI transmission and absorption cross section σ.
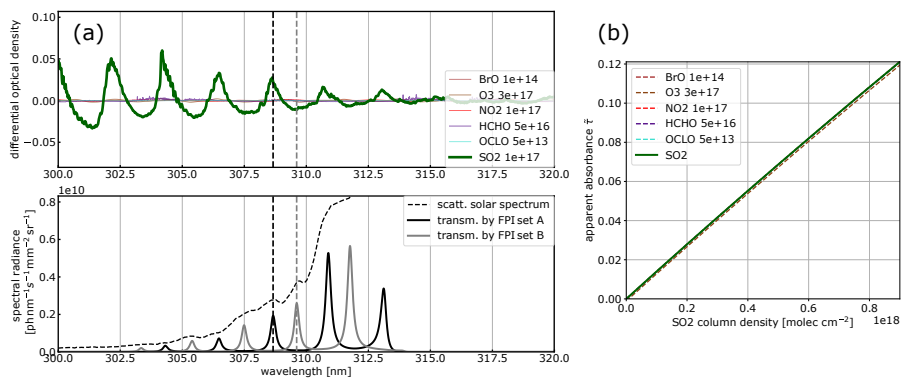

Figure 2. Model results for SO_2: (a) the differential optical densities of the assumed differential trage gas CDs are plotted in the upper panel. The lower panel shows the spectral radiance of the sky (dashed line) and the transmitted spectral radiances of the FPI and BPF (drawn lines, on-band in black, off-band in gray). (b) shows the calculated calibration curve for SO_2 only (drawn line) and with different interfering species included (dashed lines, CDs in $[\mathrm{molec\,cm^{-2}}]$ see legend and Tab. 1).
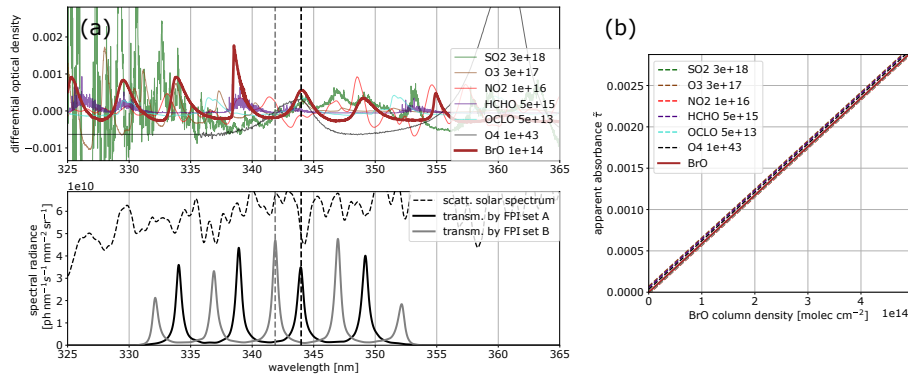
Figure 3. Model results for BrO: (a) the differential optical densities of the assumed differential trage gas CDs are plotted in the upper panel. The lower panel shows the spectral radiance of the sky (dashed line) and the transmitted spectral radiances of the FPI and BPF (drawn lines, on-band in black, off-band in gray). (b) shows the calculated calibration curve for BrO only (drawn line) and with different interfering species included (dashed lines, CDs in $[\mathrm{molec\,cm^{-2}}]$ see legend and Tab. 1).
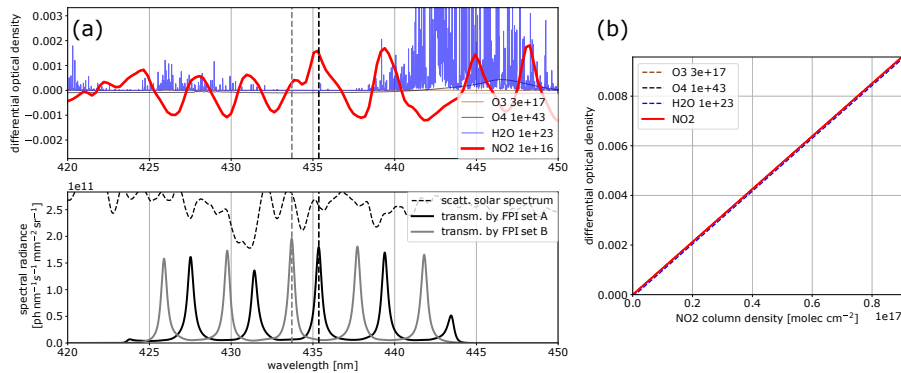

Figure 4. Model results for NO_2: (a) the differential optical densities of the assumed differential trage gas CDs are plotted in the upper panel. The lower panel shows the spectral radiance of the sky (dashed line) and the transmitted spectral radiances of the FPI and BPF (drawn lines, on-band in black, off-band in gray). (b) shows the calculated calibration curve for NO_2 only (drawn line) and with different interfering species included (dashed lines, CDs in $[\mathrm{molec\,cm^{-2}}]$ see legend and Tab. 1).
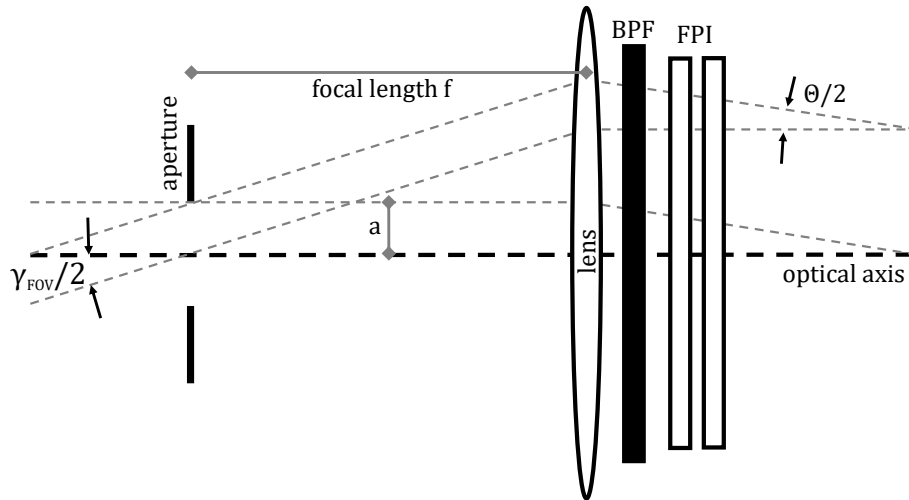
Figure 5. Image space telecentric optical setup for parallelising light from the imaging FOV before traversing the FPI and BPF.
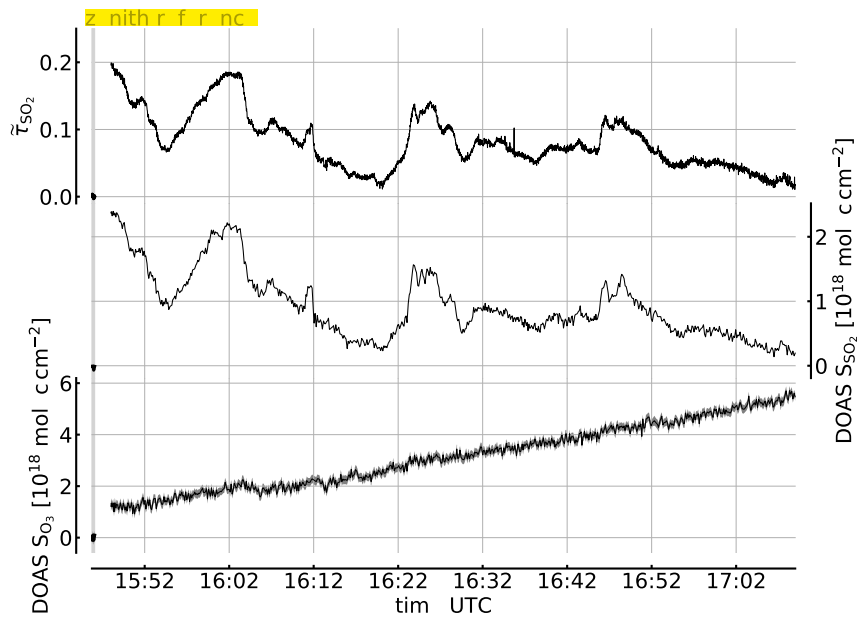

Figure 6. Time series of the apparent absorbance of the one pixel FPI Correlation Spectroscopy prototype for SO_2 detection (top trace, left scale) recorded at Etna, Sicily on 30 July 2017. A co-aligned telescope was used to simultaneously record spectra for DOAS evaluation of SO_2 and O_3 (center and bottom traces and right and bottom left scales, respectively). The apparent absorbance nicely correlates with the SO_2 CD (see Fig. 7), while no O_3 impact is observable. The growth of the retrieved O_3 differential CD is expected due to the increasing stratospheric O_3 column for increasing solar zenith angle (see text).
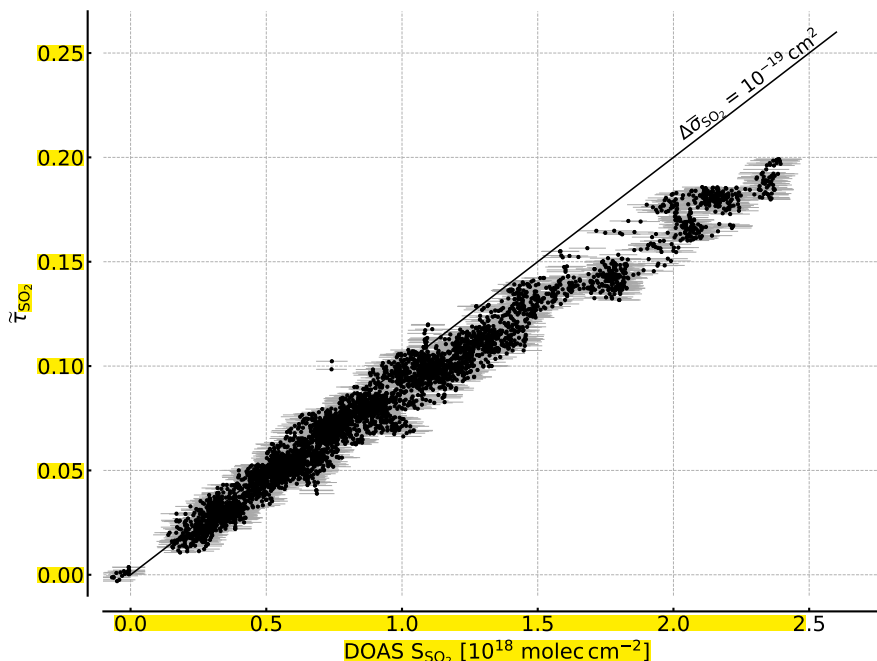
Figure 7. Correlation plot of the recorded FPI Correlation Spectroscopy apparent absorbance and the SO_2 CD retrieved by DOAS. A sensitivity of about $\Delta\overline{\sigma}_{SO_2}$ of 10^{-19} cm^2 is reached for lower SO_2 CDs. For higher CDs a flattening of the curve is observed that is induced by saturation effects due to the high SO_2 optical densities at the absorption peaks.

Table 1. Differential CDs assumed for the different measurement scenarios. The values represent high values for CD variations within a typ. imaging FOV. The targeted detection limits are indicated in bold face.

	differential CD across imaging FOV [molec cm^{-2}]		
	SO$_2$: volcanic emission (low) 300 - 315nm	BrO: volcanic emission (high) 330 - 355nm	NO$_2$: stack emission 424 - 445nm
SO$_2$	**1e17** (volcanic)	3e18 (volcanic)	-
BrO	1e14 (volcanic)	**1e14** (volcanic)	-
NO$_2$	1e17 (bgr. pollution)	1e16 (bgr. pollution)	**1e16** (stack plume)
O$_3$	3e17 (SZA change strat.)	3e17 (SZA change strat.)	3e17 (SZA change strat.)
HCHO	5e15 (background)	5e15 (background)	-
H$_2$O	-	-	1e23 (background)
OClO	5e13 (volcanic)	5e13 (volcanic)	-
O$_4$	-	1e43 (O$_2$ dimer, [molec^{2}cm^{-5}])	1e43 (O$_2$ dimer, [molec^{2}cm^{-5}]))

typical values based on: Roscoe et al. (2010); Gliß et al. (2015); Bobrowski and Giuffrida (2012); Dekemper et al. (2016); absorption cross sections:
Vandaele et al. (2009); Fleischmann et al. (2004); Bogumil et al. (2003); Serdyuchenko et al. (2014); Chance and Orphal (2011); Rothman et al. (2013);
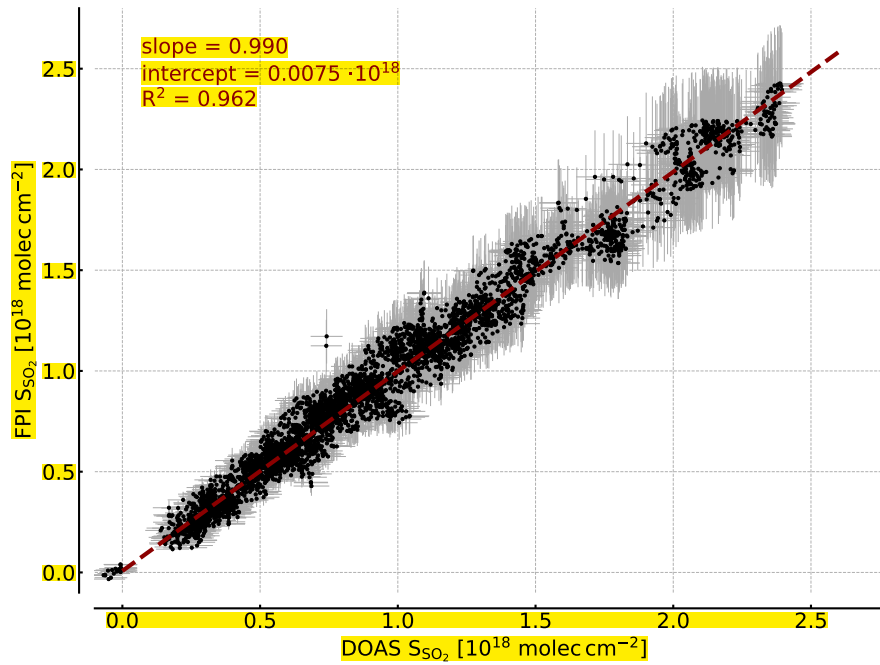Kromminga et al. (2003); Thalman and Volkamer (2013)

Figure 8. Correlation plot of the SO_2 CDs, retrieved by modeling and the SO_2 CDs retrieved by DOAS. The error bars indicate the uncertainty of the FPI finesse (3%) and the background spectral radiance in the model (10%) and the DOAS retrieval error, respectively. A high correlation is observed and the saturation effect is accounted for by the model as well.

Table 2. Instrument parameters of FPI, BPF and optical setup used for the simulations. The radiance for the on-band setting I_A at the detector was approximated based on the instrument parameters and sky radiance values from Blumthaler et al. (1996).

	instrument parameters			
	SO_2	BrO	NO_2	
d_A [µm]	21.60	11.52	23.72	FPI surface displacement setting A
d_B [µm]	21.44	11.62	23.63	FPI surface displacement setting B
R	0.7	0.7	0.7	FPI surface reflectivity
P_{BPF}	0.7	0.7	0.7	BPF peak transmission
λ_{BPF} [nm]	308	342	434	BPF central wavelength
$\delta_{\lambda,BPF}$ [nm]	10	20	18	BPF FWHM
f [mm]		50		focal length of imaging optics
Θ [°]		1		required parallelisation
a [mm]		0.44		aperture radius of imaging optics
a_{FPI} [mm]		7.5		aperture radius of FPI
η	0.25		0.5	loss factor
γ_{FOV} [°]		17		imaging FOV of camera
I_A [photons s^{-1} mm^{-2} sr^{-1}]	4.51e9	1.48e11	5.17e11	

Table 3. Simulation results: the spatial resolution of a FPI Correlation Spectroscopy measurement was calculated for an exposure time of 10 s and the target detection limits, shown in Tab. 1.

	simulation results		
	SO_2	BrO	NO_2
$\Delta\overline{\sigma}$ [cm^{-2}]	1.5e-19	6e-18	1.1e-19
target det. lim. [molec cm^{-2}]	1e17	1e14	1e16
target det. lim $\tilde{\tau}$	0.015	0.0006	0.0011
required $N_{phe,pix}$	8.9e3	5.6e6	1.7e6
required E_{pix} [mm^2 sr]	7.9e-7	1.5e-5	6.6e-7
max. spatial resolution (n_{pix} n_{pix})	**226 226**	**51 51**	**252 252**